An hybrid particle-grid method for the study of differential diffusion

Simon Santoso, Jean-Baptiste Lagaert, Guillaume Balarac, Georges-Henri Cottet

Hybrid particle-grid methods for the study of differential diffusion in turbulent flows

Simon Santoso[a], Jean-Baptiste Lagaert[b], Guillaume Balarac[c,d], Georges-Henri Cottet[a]

[a]*Laboratoire Jean Kuntzmann, Université Grenoble Alpes, Grenoble, 38000, France*
[b]*Laboratoire de Mathématiques Orsay, Université Paris Saclay, Paris, 75000, France*
[c]*Univ. Grenoble Alpes, CNRS, Grenoble INP, LEGI, Grenoble, France*
[d]*Institute Universitaire de France (IUF), Paris, France*

Abstract

This paper is devoted to the development and application of hybrid methods combining, on the one hand, semi-lagrangian methods for the advection-diffusion of scalars, and, on the other hand, either finite volume or spectral methods, depending on the flow geometry, for the Navier-Stokes equations. A particular focus is made on the accuracy and scalability of the methods. These methods are then used to study differential diffusion of scalars on two canonical cases: Homogeneous Isotropic Turbulence and a jet flow. We first characterize differential diffusion in terms of spectral distribution. We then use the Reynolds decomposition to bring out the different mechanisms involved in the energy budget of the scalar and we analyze their spatial distribution.

Keywords: Particle Method, Finite-Volume Method, Differential Diffusion, Passive Scalar

1. Introduction

The advection-diffusion of a scalar function in turbulent flows is a phenomenon that occurs in various situations. In heat transfer, the scalar function is the temperature [1]. In the context of mass-transfer, [2] investigates the concentration of gases in a canal. In combustion, the advected scalar can also be the mixture fraction between the different injected components of the mix [3]. In the case of a non-diffusive scalar, it can be captured by its level sets, which leads to the numerical treatment of multiphase turbulent flows [4].

Passively advected scalars mainly differ by their diffusivity properties characterized by the Schmidt number (or Prandtl number, when temperature is considered), the viscosity-to-diffusivity ratio.

Although direct numerical simulation is a powerful tool to predict the dynamics of scalars, the case of scalars with high Schmidt numbers remains a challenge. Indeed, for Schmidt numbers, Sc, larger than one, the Kolmogorov scale η_K, defined as the smallest variation scale of the velocity, is linked with the Batchelor scale η_B, the smallest variation scale of one scalar, by the following relation

$$\eta_B = \frac{\eta_K}{\sqrt{Sc}}. \tag{1}$$

The above relation shows that for Schmidt numbers larger than one, the scalar dynamics occurs at scales smaller than the Kolmogorov scale, whereas the range of scalar dynamics scales is smaller than the range of turbulent scales for Schmidt number smaller than one [5]. As a consequence, the accurate treatment of scalar advection-diffusion at high Schmidt numbers requires a finer mesh for the scalar than for the momentum. This is the reason why numerical studies are in general restricted to moderate Schmidt numbers (see for instance [6]).

The case of high Schmidt scalar advection-diffusion has however been treated in several papers such as [7] where authors studies several statistics of scalar with Schmidt number up to 64 and a turbulent Reynolds number equal to $R_\lambda = 140$, using a spectral method on a unique mesh. In such simulations, the velocity is clearly over-resolved. The multi-scale nature of the problem naturally leads to using two different grids to solve the Navier-Stokes equations on the one hand, and, on the other hand, the scalar advection-diffusion equations for the scalars. Gotoh et al [8] describe a method combining a spectral method for the Navier–Stokes equation and compact finite-difference schemes for simulations of decaying turbulence on

different grids. The Schmidt numbers considered in this study are 1 and 50. More recently, [9] introduced a method combining a spectral method to solve Navier-Stokes and a high order semi-lagrangian particle method to study scalars with Schmidt numbers up to 128. It was demonstrated that the CFL-free nature of the particle method and its high parallel scalability led to substantial savings over a pure spectral method achieving a comparable accuracy. The idea of using different grids for the flow and the scalar was also used in [10] for Rayleigh Benard convection in square cavities discretized by finite-differences.

These methods allow to investigate the fundamental physics of turbulent scalar transport but they are not suited to industrial applications. In this paper we extend the work of [9] to study differential diffusion in homogeneous turbulence and in jets. For the case of jets we propose a method combining a semi-lagrangian particle method with a finite-volume solver for the Navier-Stokes equations. The finite-volume solver YALES2 [11] is chosen for its good parallel performance and because it is widely used in the study of reacting flows. In order to reach high resolution with optimal efficiency, special care must be given to the parallel implementation of the particle-grid coupling. The hybrid method will be used to study the mixing of scalars in the context of Homogeneous Isotropic Turbulence and a jet flow for values of the Schmidt number higher than what was previously done.

Many studies have been devoted to the mixing of scalars in a turbulent flows [12, 13]. If two scalars are seeded in exactly the same manner, difference in their mixing dynamics are only due to the difference of their molecular diffusivity. This is the differential diffusion phenomenon [14]. Due to the molecular origin of the differential diffusion, it is expected that this phenomenon could be negligible at high enough Reynolds number. However, experimental studies show that differential diffusion persists at high Reynolds and/or Schmidt numbers [15]. The proposed hybrid approach is in particular used to better understand the differential diffusion phenomenon occurring for the mean and turbulent fields, by using quantities based on the scalar difference.

The article is structured as follows. In the first section we recall the definition of semi-lagrangian particle methods for transport equation. We define the coupling with finite-volume solvers and its parallel implementation. In section 3 we discuss the accuracy and the computational efficiency of the hybrid method compared to a pure finite-volume method. Finally, in section 4 we apply the hybrid method to study differential diffusion in two

configurations : first, in the case of homogeneous turbulence,with a particle spectral hybrid method along the lines of [9], then, in the case of a jet flow, with the hybrid particle finite-volume method.

2. Numerical methods and parallel implementation

In this section some details are given about the numerical method used to solve the coupled system equations, and their implementation.

For incompressible flows, the dynamics of the flow is governed by the Navier-Stokes equations,

$$\frac{\partial \mathbf{v}}{\partial t} + \mathbf{v} \cdot \nabla \mathbf{v} = -\nabla \left(\frac{p}{\rho} \right) + \nu \Delta \mathbf{v} \tag{2}$$

$$\nabla \cdot \mathbf{v} = 0 \tag{3}$$

with $\mathbf{v}$ the velocity field, p the pressure field, and ν and ρ the viscosity and the density, respectively. The dynamics of a passive scalar, θ, seeded in the flow is governed by a advection-diffusion equation,

$$\frac{\partial \theta}{\partial t} + \mathbf{v} \cdot \nabla \theta = \kappa \Delta \theta \tag{4}$$

where κ is the diffusion coefficient of θ. The Schmidt number is then defined as $Sc = \nu/\kappa$.

As previously said, for Schmidt number larger than one the scalar dynamics develops at smaller scales than the scales of fluid motions, i.e. the Kolmogorov scale, defined as the smallest length of the turbulent motion, is larger than the Batchelor scale, defined as the smallest length of scalar fluctuations. This motivates the use of different grids to solve scalar and flow equations. In this work, the scalar advection-diffusion equation (4) is solved on a fine cartesian mesh while Navier-Stokes equations (2) and (3) are solved on a coarser (structured or unstructured) mesh. Note that in the case where several scalars are advected, the size of the scalars mesh is driven by the scalar with the highest Schmidt number as its Batchelor scale will be the smallest.

In this work, the Navier-Stokes equations are solved using an Eulerian approach with either pseudo-spectral method as in [9], or a finite-volume method on unstructured meshes. To overcome an additional CFL constraint due to the use of a fine mesh, a semi-lagrangian particle method is used for the scalar transport.

2.1. Semi-lagrangian particle methods

The principle of semi-lagrangian particle methods is to concentrate the transported quantity θ on a set of particles. Starting from a set of particles initially located on a cartesian and uniform grid, the advection phenomenon is first simply taken into account by moving the particles using the local advection velocity field. To avoid accuracy issues with the particles distortion in space, the particles are remeshed after each time-step on the original grid using an interpolation kernel with good conservation and regularity properties.

If θ_j^n and θ_j^{n+1} denote scalar values at grid points for two successive time-steps, the method is summarized by the following formula

$$\theta_i^{n+1} = \sum_{j \in \mathcal{P}} \theta_j^n \Lambda\left(\frac{\mathbf{x}_i - \tilde{\mathbf{x}}_j}{\Delta x^\theta}\right) \quad , \quad i \in \mathcal{P}, \tag{5}$$

where $\mathcal{P}$ is the particle set, $\mathbf{x}_i$ is the position of the i-th grid points, $\tilde{\mathbf{x}}_j$ is the position of the particle j after one advection step, Δx^θ is the grid size and Λ is the remeshing kernel. These methods have been extensively used for the transport of vorticity in 2D and 3D flows (see [16, 17, 18] and the references therein). For the transport of scalar they have been analyzed and validated in [19].

Semi-lagrangian particle methods are conservative and avoid CFL stability conditions.The time-step limitation only depends on the maximal strain in the flow $|\nabla u|_\infty$, independently of the grid size. It reads

$$\Delta t \leq \frac{1}{|\nabla u|_\infty}. \tag{6}$$

Their order of convergence depends on the regularity and moment conservation of the considered kernel. Kernel formula have been derived in [19]. In this paper we use a second order kernel originally given in [20]. It is given by tensor products of the one-dimensional following formula :

$$\Lambda(x) = \begin{cases} \frac{1}{12}(1-|x|)(25|x|^4 - 38|x|^3 - 3|x|^2 + 12|x| + 12) & \text{if } 0 \leq |x| < 1 \\ \frac{1}{24}(|x|-1)(|x|-2)(25|x|^3 - 114|x|^2 + 153|x| - 48) & \text{if } 1 \leq |x| < 2 \\ \frac{1}{24}(3-|x|)^3(5|x|-8)(|x|-2) & \text{if } 2 \leq |x| < 3 \\ 0 & \text{otherwise} \end{cases} \tag{7}$$

As Λ has a compact support, the algorithm can be implemented in a parallel manner to optimize the computational cost. This topic is addressed below.

Since particles are on a cartesian grid at each time-step, diffusion or source terms can easily be handled in a time-splitting fashion using classical finite-differences.

Finally, note that semi-lagrangian particle methods can be implemented together with adaptive mesh refinement strategies in order to further enhance their adaptivity by optimizing particle spacing as a function of the local variations of the scalar [21, 20]. In particular, particle refinement can be obtained through wavelet based multi-resolution analysis which can provide a high degree of compression and further reduce the computational cost.

2.2. Hybrid method

In this work, the resolution of scalar transport equations by a semi-lagrangian particle method is coupled with the resolution of Navier-Stokes equations using an Eulerian approach. To consider turbulent mixing at high Schmidt numbers, a finer grid can be used for the scalar transport than for the flow fields. This hybrid approach benefits from the stability of semi-lagrangian particle method. As already mentioned, the time-step is only limited by the maximul strain and not by a CFL condition depending on the grid-size. In practice that means that the time-step is only constrained by the grid-size of the flow solver.

In the applications considered in section 4, the Navier-Stokes equations are solved either by a pseudo-spectral method or by a finite-volume method. The coupling of a pseudo-spectral method with a semi-lagrangian particle method has been described and thoroughly validated in [9], both from the point of view of accuracy and computational efficiency. The main issues of the coupling, velocity interpolation for particles advection and the parallel implementation, highly benefit from specific features of spectral methods. In particular, for pseudo-spectral methods the mesh is uniform and cartesian. The domain decomposition between processes is thus algebraic and structured. Moreover, the scalar mesh is only a uniform refinement of the mesh used for velocity computation and spectral interpolation from a cartesian mesh to another is straightforward. This choice of interpolation ensures an interpolation error that decreases exponentially fast with respect to the grid size.

We now focus on an hybrid method combining a finite-volume solver and a semi-lagrangian particle method, something which, to our knowledge has never been done. The Navier-Stokes equations are solved with the so-called

YALES2 pair-based finite-volume solver. This solver uses a tetrahedral mesh and a node-centered approach. The control volumes are the cells of the dual mesh, generated by computing the barycenter of each cell of the primal mesh [11]. The unknowns are classically the average of the advected quantities over the control volume. This approach leads to a second-order accurate scheme on structured meshes. It is stable under the following CFL condition

$$|u|_\infty \Delta t \leq 0.9 \Delta x \tag{8}$$

We refer the reader to [22] for more details.

The Navier-Stokes equations are solved thanks to a two steps prediction-correction method [23]. The first step consists in the advection of each averaged quantity at the flow velocity. The time integration for this step is made with a Runge-Kutta-like fourth-order scheme TFV4A [24]. As a result of this step an intermediate velocity field $\mathbf{v}^*$ is computed. The second step consists in the correction of the pressure field p by solving the following Poisson problem :

$$\nabla \cdot \frac{1}{\rho} \nabla p = \frac{1}{\Delta t} \nabla \cdot \mathbf{v}^* \tag{9}$$

Equation (9) can be solved with several methods. For instance, [25] uses a BiCGStab algorithm, while [26] use a deflated preconditionned conjugate gradient method. This latter method will be used in the present work.

The coupling with the semi-lagrangian method for the scalar transport follows the description done in [9] by replacing the spectral interpolation by a linear interpolation: particles are created on each scalar nodes of a cartesian mesh, then advected using a linear interpolation of the velocity and a second-order Runge-Kutta integrator and finally remeshed on the scalar mesh. Note that using second order linear interpolation is consistent with the order of the remeshing kernel.

Scalar diffusion is done on the grid using a classical second-order 7-points finite-difference scheme and an explicit time-advancing scheme. This results in the following stability condition :

$$\Delta t < \frac{1}{6} \frac{\kappa}{\Delta x^2} \tag{10}$$

In practice, in our applications the values of the diffusivity coefficients κ are small enough to ensure that this condition is not more restrictive than the CFL condition imposed on the finite-volume solver for the Navier-Stokes equations.

Since in our study there is no feedback of the scalars to the flow, the accuracy of the hybrid method can be deduced from that of the underlying finite-volume and particle methods. Overall, the hybrid method is second order in space and first order in time. It is stable for a time-step satisfying the conditions (6), (8), (10).

2.3. Parallel implementation

Starting from a distributed coarse mesh that discretizes the spatial domain and is used to compute the velocity, a cartesian and possibly finer mesh is created to solve the advection equations. Scalar nodes are added in a cartesian fashion: $x_{ijk} = (i\Delta x, j\Delta y, k\Delta z)$. Virtual particles are then created on each of those scalar nodes and moved with the flow velocity. The location of x_{ijk} inside the coarse mesh is thus needed to interpolate the velocity at x_{ijk} from the unstructured mesh. As a consequence, an element K of the unstructured mesh of velocity and the set of scalar nodes contained in K must be handled by the same processor (constraint C1). Finally, the advected particles are communicated to the processor which handle the element which contains them and remeshed on the fine cartesian grid.

As a consequence of C1, the domain decomposition for the cartesian mesh must follow the unstructured decomposition of the finite-volume mesh.

The particle remeshing and the diffusion term may involve large stencils (6 grid points in each direction in the simulations of the section 4.3). In order to manage them efficiently, ghost nodes are added at the boundaries between two processes (constraint C2). The remeshing is done in these ghost nodes which are then synchronized by MPI communications. This is all the more complex as the decomposition is not algebraic and that the association of these ghosts to their only physical node is non trivial.

Figure 1 illustrates constraint C1. In particular, the four nodes marked by a cross are located, within rounding error, at the boundary between two processes. Two cartesian nodes coincide with node B and D of the finite-volume mesh, two are on a finite-volume edge. In order to avoid artificially introducing a scalar source term, a single particle must be created at this point. To do so, those ghost scalar nodes must be created in a single copy, for example on the lowest rank process that could accommodate it. If the node is duplicated, so are the particles, and, for the remeshing step, the value of the scalar associated with this node will be added several times as each copy of the particle is remeshed. For point A, it is the first process.

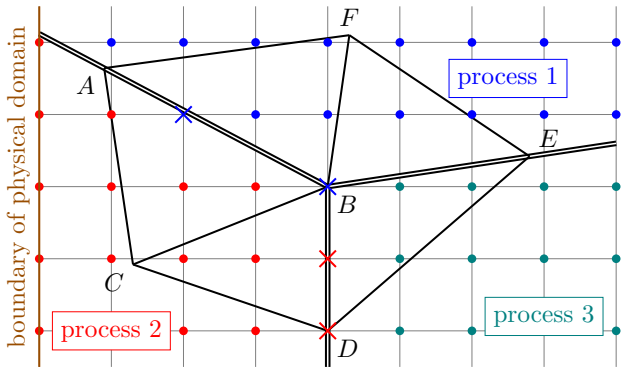

Figure 1: Distribution of particles nodes in the finite-volume domain partition. Letters stands for finite-volume nodes. Scalar nodes are marked by a circle ; scalars nodes near process boundaries are marked by a cross. The colors match the hosting processes.

From the implementation point of view, we must determine if the cartesian node is near a finite-volume node, edge or face and then use the communicator defined on the node/edge/face of the unstructured mesh to obtain the list of the processes that could host this node. Then all these processes choose the one with the lowest rank (without additionnal communication) and then make sure that the chosen node does indeed host this node.

As for the C2 constraint, Figure 2 illustrates the ghost nodes to be created. The difficulty lies in the creation of a communicator allowing to synchronize the ghost nodes and the "real" associated nodes. To do this, one needs to know which process contains the "real" node associated with it. This step is done using the particle relocation algorithm natively implemented in YALES2. This algorithm was originally defined to track physical particles in the flow [27].

Several remarks can be done here. Particles are not created on ghost nodes ; ghosts are only used during particle remeshing. The partition of the scalar nodes set is extremely dependent on the partition of the element set. As a consequence, a load balancing problem can appear if the element set is poorly distributed among the processors. Domain decomposition is performed by the Metis library. It is based on the number of cells of the finite-volume mesh. We will see in section 3.2 that in some situations this decomposition is successful. However, as we will see in section 4.3, in highly non homogeneous cases the load balancing can significantly deteriorate.

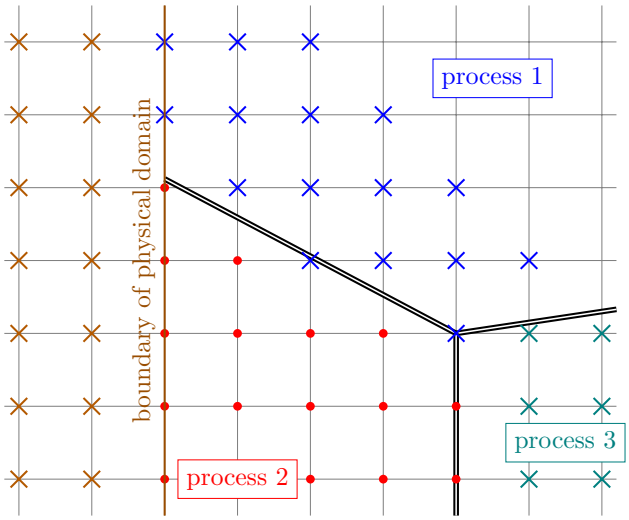

Figure 2: Distribution of particles ghost nodes. The physical nodes are marked by a circle, the ghosts of process 2 by a cross of the color of the process that contains the associated physical node. The brown ghost nodes are supported via the boundaries conditions. For the sake of simplicity, the width of the half stencil is fixed at 2 in this illustration.

3. Accuracy and computational efficiency

A set of numerical experiments are now performed to assess the accuracy and the efficiency of the proposed approach. As we already said, the hybrid method combining a pseudo-spectral and a semi-lagrangian particle methods have been studied in [9]. We focus here on the transport equation, solved either by a semi-lagrangian method or the finite-volume method implemented in YALES2 for the advection-diffusion equation. We first compare the accuracy of these two methods, then their computational cost. We finally measure the parallel scalability of the full hybrid method which combines the finite-volume solution to the Navier-Stokes equations and the semi-lagrangian particle method to advect the scalar.

3.1. Accuracy

To compare the accuracy of semi-lagrangian particle method with the finite-volume method implemented in YALES2, we consider a cube of size 2π with periodic boundary conditions. The finite-volume mesh is obtained by perturbation (shaking) of a uniform tetrahedral mesh. The particle mesh is a uniform cartesian grid. We impose the following velocity field $\mathbf{u}$ on the

finite-volume mesh, and scalar initial distribution on the particle mesh,

$$\begin{aligned} \mathbf{u}_x &= \sin(x)\cos(y)\cos(z), \\ \mathbf{u}_y &= -\cos(x)\sin(y)\cos(z), \\ \mathbf{u}_z &= 0, \end{aligned} \tag{11}$$

$$\theta(\mathbf{x}, 0) = \cos(8x)\cos(8y)\cos(8z). \tag{12}$$

Three grid sizes are considered for the scalar mesh with number of elements $N_\theta = 128^3, 256^3$ and 384^3. For the particle method, the velocity at scalar nodes is obtained thanks to a linear interpolation from the velocity field given on a 128^3 cartesian mesh, and particles are advected with a fourth order Runge-Kutta scheme. For these grid resolutions we monitor the decay of the scalar variance θ_{RMS} :

$$\theta_{\text{RMS}} = \left(\frac{1}{V} \int_V \theta^2 dV \right)^{1/2}$$

and its time-derivative. The value of the latter quantity, which should correspond to the physical dissipation, is a good indicator of the numerical dissipation produced by the methods. Those decays are compared to a reference solution obtained by a pseudo-spectral method. Two different diffusivity coefficients for θ will be considered : $\kappa = 6.6\,10^{-3}$ (case 1) and $\kappa = 8.3\,10^{-4}$ (case 2).

For case 1, Figure 3 shows that both methods give accurate dissipation rates even at the lowest resolution.

For case 2, with a smaller scalar diffusivity, one can observe on the top pictures of Figure 4 that the finite-volume method has troubles to converge to the reference solution. By contrast, Figure 5 and Figure 6 show that the semi-lagrangian method gives at the lower resolution results that are comparable to the higher resolution finite-volume simulation. We also note that the semi-lagrangian method is actually at the lowest resolution slightly under-dissipative, a feature which is often shared by high order methods.

3.2. Computational Cost

To measure the efficiency of the hybrid method in terms of computational cost, we now consider the case when the velocity is given by the finite-volume

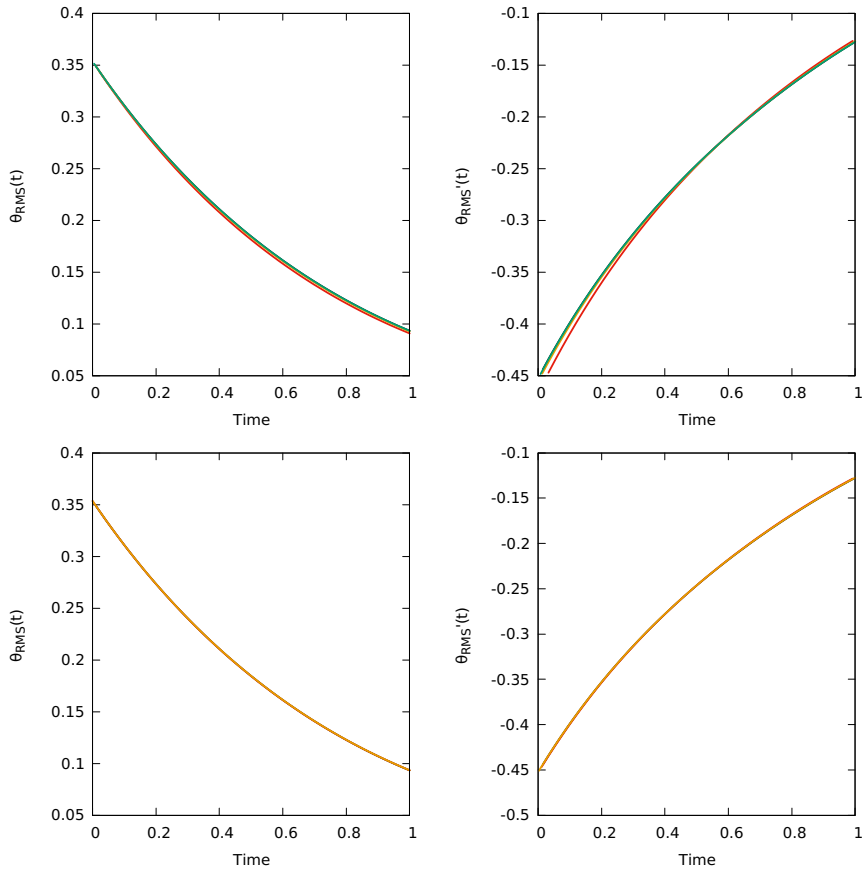

Figure 3: Comparison of finite-volume and semi-lagrangian methods with the reference solution (black) for the test case (11) with $\kappa = 6.6\,10^{-3}$. Top (resp bottom) pictures show results for the pure finite-volume method (resp semi-lagrangian method). Grid sizes are 128^3(red), 256^3(orange) and 384^3(green). Left pictures : scalar RMS, right pictures : time-derivative of scalar RMS.

Navier-Stokes solver and we compare the hybrid method with a full finite-volume method, that is a method where both the Navier-Stokes equations and the scalar transport equations are solved by the finite-volume solver of YALES2.

The velocity field is initialized with the formulas (11). The viscosity is equal to $\nu = 5\,10^{-3}$ which corresponds to a Reynolds number equal to $Re = \frac{U_{\max \times 2\pi}}{\nu} \simeq 1256$. We set the Schmidt number equal to 6, which corresponds to the diffusivity coefficient of the second test case in the previous subsection. In light of what was seen above, a grid of 128 points in each

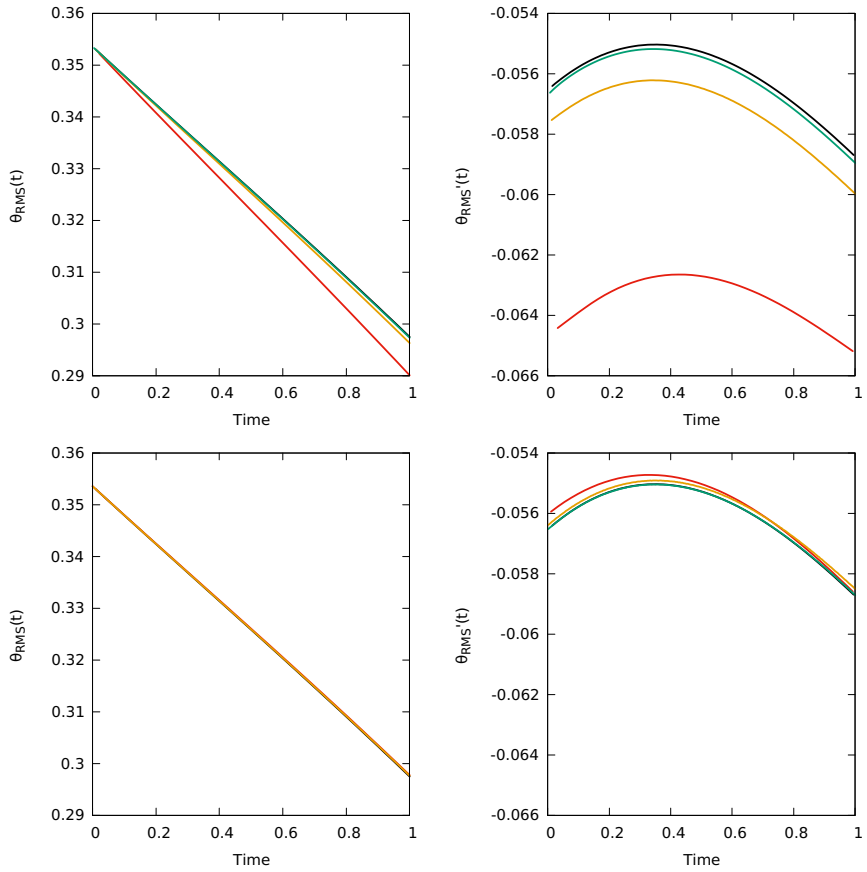

Figure 4: Comparison of finite-volume and semi-lagrangian methods with the reference solution (black) for the test case (11) with $\kappa = 8.3\,10^{-4}$. Top (resp bottom) pictures show variance of the scalar and its time derivative for the pure finite-volume method (resp semi-lagrangian method). Grid sizes are 128^3 (red), 256^3 (orange) and 384^3 (green). Left pictures : scalar RMS, right pictures : time-derivative of scalar RMS.

direction is sufficient for the DNS of the Navier-Stokes equation by the finite-volume method. For the scalar transport a grid of 128^3 points would be enough for the particle method whereas the finite-volume solver would require a grid of 384^3 to achieve a similar accuracy.

We measure the time per iteration for 128^3, 256^3 and 384^3 particles, compared to the finite-volume method using 384^3 grid points (see Table 1). For that test, simulations were run on 100 CPU cores. We observe that the higher resolution case shows a slight overhead for the hybrid method, due

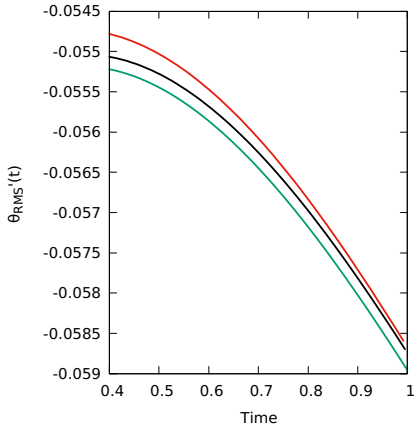

Figure 5: Comparison, for the time derivative of the scalar RMS, of the reference solution (black), the finite-volume result with $N = 384^3$(green) and the semi-lagrangian result with $N = 128^3$ (red).

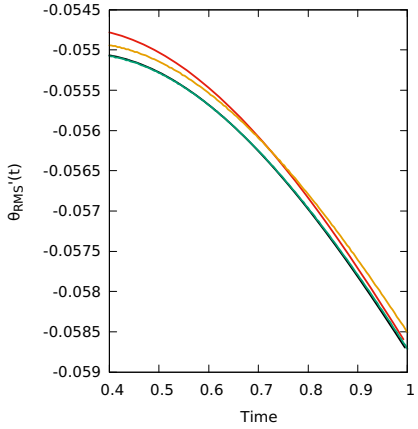

Figure 6: Close up of the bottom right picture of Figure 4.

to the interpolations needed in the algorithm. The lower resolution case shows a factor 7 speed up for the particle method. Given that the time-step of the particle method is related to the velocity strain, which itself is controlled by the grid resolution used to solve the Navier-Stokes equation, we obtain for the hybrid method using 128^3 grid points an additional factor 3 speed up over the 384^3 finite-volume method can be expected. This roughly leads to an overall factor 20 speed-up over a full finite-volume solver yielding comparable accuracy. In future work we will combine the semi-lagrangian

particle algorithm with directional splitting, along the lines of [19], which will further reduce its computational time.

These results show that the hybrid method can be seen as a good alternative to the pure finite-volume method. Note however that in the case presented here, because the finite-volume and particle meshes are uniform, the load balancing, based on partitioning of the finite-volume mesh, is also optimal for the particle distribution on the cartesian mesh. We will see in the application dealing with a jet that this is not always the case.

Method	Velocity Grid size	Scalar Grid size	Time per iteration [s]
Finite-Volume	384^3	384^3	3.50
Semi-lagrangian	128^3	128^3	0.52
	128^3	256^3	1.41
	128^3	384^3	4.28

Table 1: Comparison of time per iteration for finite-volume and semi lagrangian method for several grid size and 100 CPUs.

3.3. Parallel scalability

Figure 7 shows the strong and weak scalability of the hybrid method. The strong scalability was studied using 512^3 and 1024^3 particles. In both cases, the Navier-Stokes equations were solved on a 256^3 grid. The number of cores ranges between 128 and 1526. We note that for 512^3 particles, the strong scaling (top picture of Figure 7) deteriorates beyond 512 cores, diue to communications between processors. As expected, this problem tends to disappear for 1024^3 particles and the scaling is almost perfect up to 1536 cores.

The weak scaling was performed starting from a tetrahedral mesh with 256^3 velocity elements and 512^3 particles. Since [11] already demonstrated the good scalability of the fluid solver, we only consider the semi-lagrangian part of the algorithm. We increase the number of particles from 512^3 particles to 930^3. The bottom picture of Figure 7 shows that the time of one iteration remains almost constant up to 1536 cores.

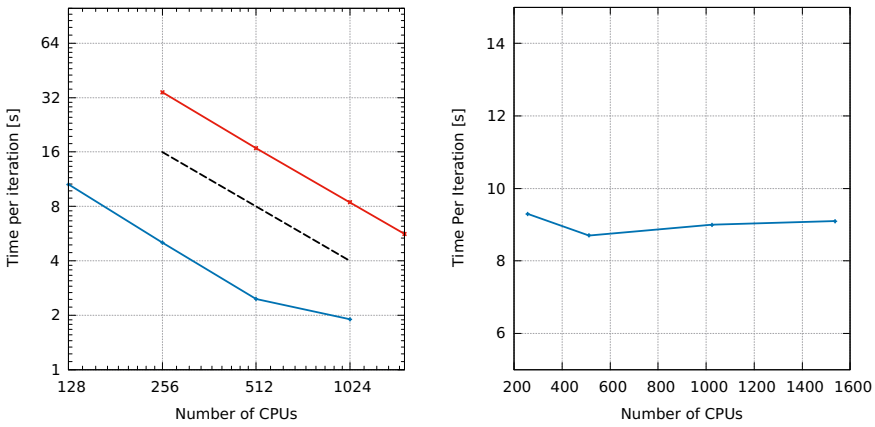

Figure 7: Left picture : weak scaling for the hybrid method. The blue line shows the time of one iteration for 512^3 particles and the red line for 1024^3 particles. The black dashed line shows the perfect scaling. Right picture : shows weak scaling for the hybrid method for a number of processors ranging from 256 to 1536.

4. Application to the differential diffusion of passive scalars

This section is now dedicated to the study of differential diffusion. Various experimental [28, 29, 15] and numerical [30, 31, 32, 33] studies have been devoted to the differential diffusion process, mainly in homogeneous isotropic turbulence (HIT), and turbulent jet configurations. In these works, the differential diffusion is characterized by various quantities. First the correlation coefficients between scalars or between scalar gradients can be considered. These quantities decay until complete decorrelation for decaying (unforced) scalar [34], whereas non-zero coefficients value are obtained at steady state when a mean scalar gradient forcing is used [31]. This asymptotic value is found to be only dependent of the ratio of Schmidt numbers of the couple of the scalars under consideration [31, 33, 34, 35], showing that the differential diffusion increases with this ratio. The differential diffusion can also be characterized by another scalar field, defined as the difference between the scalars [36]. The variance of this scalar difference has been considered. It decays with the Reynolds number. The decay of the scalar difference variance is predicted as a power law of the Reynolds number, but different values of the exponent have been proposed [35, 36, 37]. The spectrum of the scalar difference has also been intensively studied in previous works. This spectrum is found to decrease for all wavenumbers for unforced mixing [34] and turbulent jet configurations

[38, 15]. However, for scalar fields forced by a mean scalar gradient, the scalar difference spectrum increases at small wavenumber and decreases at high wavenumbers, with the presence of a peak [31, 37]. This confirms that the phenomenon of differential diffusion is fundamentally dependent on the nature of the underlying flow field [38] or the nature of the mixing condition (forced or not) [30]. The forcing term allows to limit the differential diffusion to small scales, whereas without forcing the effects are propagated from small to large scales. Moreover, the range of scales of the differential diffusion is found to increase with the Schmidt numbers ratio [33]. Finally, in terms of scales transfer, the differential diffusion phenomenon is mainly dominated by local transfers, even if non-local transfers could increase with the values of the Schmidt number [39, 33].

4.1. Equations for quantities based on the scalar difference

In the present work, the proposed hybrid method is used to study differential diffusion phenomenon for values of the Schmidt number ratio higher than previously reported in literature, in two different canonical flow configurations: homogeneous isotropic turbulence (HIT) and transitional round jet. The differential diffusion is mainly characterized by quantities based on the scalar difference.

Let us consider two scalars θ_α and θ_β, seeded in exactly the same manner but with different molecular diffusivities, κ_α and κ_β, respectively. Their governing equation are given by equation (4), and their mixing dynamics will differ only due to the difference of their molecular diffusivity. The proposed analysis is mainly devoted to the characterization of the scalars difference, $z = \theta_\alpha - \theta_\beta$.

From the scalars transport equation, the governing equation of z can be written as,

$$\frac{\partial z}{\partial t} + \nabla \cdot (z\mathbf{v}) = S\Delta z + D\Delta w, \tag{13}$$

with $w = \theta_\alpha + \theta_\beta$, $S = \frac{\kappa_\alpha + \kappa_\beta}{2}$, and $D = \frac{\kappa_\alpha - \kappa_\beta}{2}$. Note that this equation is original and slightly different from the form used by Hunger *et al.* [6] or Bilger and Dibble [36]. This allows to define without ambiguity the diffusion and source terms, which depend both on the the molecular diffusivity on the scalars. The scalar difference, z, is solution of a scalar advection-diffusion transport equation with a diffusivity coefficient equal to S, and with an additional source term, $D\Delta w$. The evolution of z can be studied from an

energy point of view by studying z^2 (by analogy with the kinetic energy, $\frac{1}{2}\mathbf{v}\cdot\mathbf{v}$, for the velocity field). The governing equation of z^2 reads as

$$\frac{\partial z^2}{\partial t} = \underbrace{\nabla\cdot\left(S\nabla z^2 + 2Dz\nabla w - \mathbf{v}z^2\right)}_{\text{Diffusion}} \underbrace{-2S\nabla z\cdot\nabla z}_{\text{Dissipation}} \underbrace{-2D\nabla z\cdot\nabla w}_{\text{Production}}. \tag{14}$$

This allows to define without ambiguity diffusion, dissipation and production terms, which depends on both molecular diffusivities.

Defining the last term as a production term needs some discussion. To highlight the role of this term, let us consider a large enough volume to assume no scalar flux at the boundaries of this volume. By integrating equation (14) on this volume, we can consider the global equilibrium of the differential diffusion process. The left-hand-side of this equations represents the time variation of the integration of z^2 in the considered volume, which is in equilibrium with diffusion, dissipation and source terms. The diffusion terms can be grouped in a divergence form meaning that their integration over the considered volume will be equal to zero. This shows that these terms do not participate in the global balance, but only act as spatial re-distribution. Conversely, the dissipation term, $-2S\nabla z\cdot\nabla z$, is always negative meaning that this term will lead to a decrease of the differential diffusion process. In a steady state, the last term should be a production term, with a positive integral, to lead to a global equilibrium between production and dissipation. A phenomenological argument can be given to discuss the sign of the production term. Indeed, the production term also reads

$$-(\kappa_\alpha-\kappa_\beta)\nabla z\cdot\nabla w = -(\kappa_\alpha-\kappa_\beta)\left((\nabla\theta_\alpha)^2-(\nabla\theta_\beta)^2\right). \tag{15}$$

In the case $\kappa_\alpha > \kappa_\beta$, for example, that is when the scalar θ_α is more diffusive than the scalar θ_β, it can be expected that the scalar gradient of θ_α has a smaller magnitude than the gradient of θ_β. Since $\kappa_\alpha-\kappa_\beta>0$, it can thus be expected that $-(\kappa_\alpha-\kappa_\beta)\left((\nabla\theta_\alpha)^2-(\nabla\theta_\beta)^2\right)$ is mainly positive, and that the term acts as a global production term.

In this work, to characterize the effect of turbulence on this quantity, the Reynolds decomposition is also adopted : $z=\langle z\rangle + z'$, with $\langle z\rangle$ the averaging of z, and z' the fluctuation. The turbulent field will be characterized by $\langle z'^2\rangle$. Since $\langle z^2\rangle = \langle z\rangle^2 + \langle z'^2\rangle$, considering the governing equation of $\langle z\rangle^2$ and $\langle z'^2\rangle$ will allow to characterize the differential diffusion phenomenon occurring for the mean and turbulent fields, and their transfer.

The governing equation of $\langle z \rangle^2$ reads as

$$\begin{aligned}\frac{\partial \langle z \rangle^2}{\partial t} =& \nabla \cdot \left(S \nabla \langle z \rangle^2 + 2D \langle z \rangle \nabla \langle w \rangle - \langle \mathbf{v} \rangle \langle z \rangle^2 - 2 \langle z \rangle \langle \mathbf{v}' z' \rangle \right) \\ & - 2S \nabla \langle z \rangle \cdot \nabla \langle z \rangle - 2D \nabla \langle z \rangle \cdot \nabla \langle w \rangle + 2 \langle \mathbf{v}' z' \rangle \cdot \nabla \langle z \rangle,\end{aligned} \tag{16}$$

whereas the governing equation of $\langle z'^2 \rangle$ reads as

$$\begin{aligned}\frac{\partial \langle z'^2 \rangle}{\partial t} =& \nabla \cdot \left(S \nabla \langle z'^2 \rangle^2 + 2D \langle z' \nabla w' \rangle - \langle \mathbf{v} \rangle \langle z'^2 \rangle - \langle \mathbf{v}' z'^2 \rangle \right) \\ & - 2S \langle \nabla z' \cdot \nabla z' \rangle - 2D \langle \nabla z' \cdot \nabla w' \rangle - 2 \langle \mathbf{v}' z' \rangle \cdot \nabla \langle z \rangle.\end{aligned} \tag{17}$$

This governing equation show the scalar energy balance for the mean and turbulent fields respectively. Similarly to equation 14), diffusion, dissipation and production terms can be identified. Moreover, an additional term, $2\langle \mathbf{v}' z' \rangle \cdot \nabla \langle z \rangle$ appears with opposite signs in both equations. This term acts as the transfer term between mean and turbulent fields. This is a key term to understand turbulence influence on the mean field for differential diffusion.

4.2. Differential diffusion phenomenon in Homogeneous Isotropic Turbulence

4.2.1. Flow configuration

The first flow configuration consists in a forced homogeneous isotropic turbulence, using a random forcing applied at a low wave number [40] to maintain kinetic energy. The hybrid method coupling a pseudo-spectral method for the flow dynamic, with the semi-lagrangian particle method for scalars is used in this case. Four Reynolds numbers based on the Taylor microscale are considered: $R_\lambda = 30$, 55, 90 and 180. The simulation parameters are chosen such that $k_{\max} \eta_K > 1.5$ where $k_{\max}$ is the maximum wavenumber in the domain, and η_K is the Kolmogorov scales [41]. This leads to a discretization in the pseudo-spectral method using N_u^3 grid points, with $N_u = 64$, 128, 256 and 512 for the four Reynolds numbers under consideration, respectively. Figure 8 shows the kinetic energy spectra of the four considered Reynolds numbers. The spectra are normalized by the classic Kolmogorov scaling, with ϵ the kinetic energy dissipation rate. The highest Reynolds number allows to obtain an inertial range with a $k^{-5/3}$ law over one decade. For each Reynolds number, four passive scalar are considered with Schmidt numbers, $Sc_1 = 3/16$, $Sc_2 = 3/4$, $Sc_3 = 3$ and $Sc_4 = 12$ respectively. In order to resolve the scales corresponding to the highest Schmidt number, the particle grid uses N_θ^3 grid points with $N_\theta = 4N_u$.The initial scalar field is the same in all

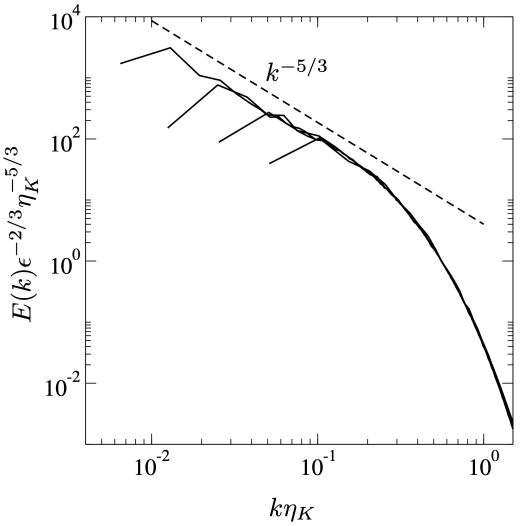

Figure 8: Normalized kinetic energy spectra for Reynolds numbers $R_\lambda = 30$, 55, 90 and 180. Increasing Reynolds numbers go with increasing inertial ranges.

these experiments [42]. To enforce a stationary scalar field, a mean scalar gradient is imposed [39]. Figure 9 shows the instantaneous scalar field, at $R_\lambda = 180$, for the Schmidt numbers Sc_2 and Sc_4 to characterize the difference of the range of turbulent mixing scales.

This database is next used to study the differential diffusion phenomenon for various Reynolds numbers and various Schmidt numbers ratios. The Schmidt number ratios are defined as $R_{Sc} = Sc_\alpha/Sc_\beta$, with $Sc_\alpha > Sc_\beta$. With the DNS database, three Schmidt numbers ratios can be considered: three couples of Schmidt numbers lead to $R_{Sc} = 4$: $(3/16, 3/4)$, $(3/4, 3)$ and $(3, 12)$; two couples of Schmidt numbers lead to $R_{Sc} = 16$: $(3/16, 3)$ and $(3/4, 12)$, and the couple of Schmidt numbers $(3/16, 12)$ leads to $R_{Sc} = 64$. The hybrid method allows to consider differential diffusion phenomenon at Reynolds numbers, Schmidt numbers and Schmidt number ratios higher than previously reported in literature.

4.2.2. Statistical characterization of the differential diffusion phenomenon

Figure 10 shows classical statistical characterization of the differential diffusion. First, figure 10 (left) shows the correlation coefficients of the gradients of scalars as a function of the Schmidt numbers ratio. This correlation is

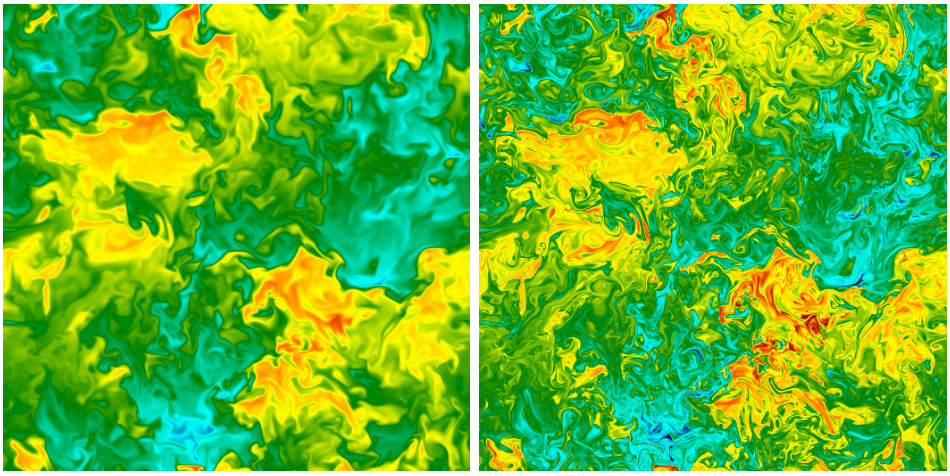

Figure 9: Planar cross-section of the flow colored by the instantaneous scalar fields at two different Schmidt number, $Sc = 3/4$ (left) and $Sc = 12$ (right) for $R_\lambda = 180$.

defined as,

$$g_{\alpha,\beta} = \frac{\langle \nabla\theta_\alpha \cdot \nabla\theta_\beta \rangle}{||\langle \nabla\theta_\alpha \rangle|| ||\langle \nabla\theta_\beta \rangle||} \tag{18}$$

where the bracket operator consists in the spatial averaging. This correlation coefficient is only controlled by R_{Sc}, independently of the Reynolds number and of the values of the Schmidt numbers. The decorrelation is more and more pronounced when R_{Sc} increases. This results has been previously established by Yeung [31] and Fox [35], by modeling this correlation coefficient as,

$$g_{\alpha,\beta} = 2\left(R_{Sc} + \frac{1}{R_{Sc}} + 2\right)^{-1/2}, \tag{19}$$

based on the stationarity and homogeneity of the scalar mixing. The DNS results are in perfect agreement with this model. This validates the model at high Schmidt number ratios and confirms the independence of this quantity with the Reynolds number on a larger range of values.

To analyze more in depth the differential diffusion phenomenon, spectra of the scalar difference variance can be considered. Figure 10 (right) shows the scalar variance spectra for both scalars with $Sc = 12$ and $Sc = 3/16$ at $R_\lambda = 180$, and the variance spectrum of the scalar difference, z, between these two scalars. Both scalars have first an inertial-convective range, and the scalar

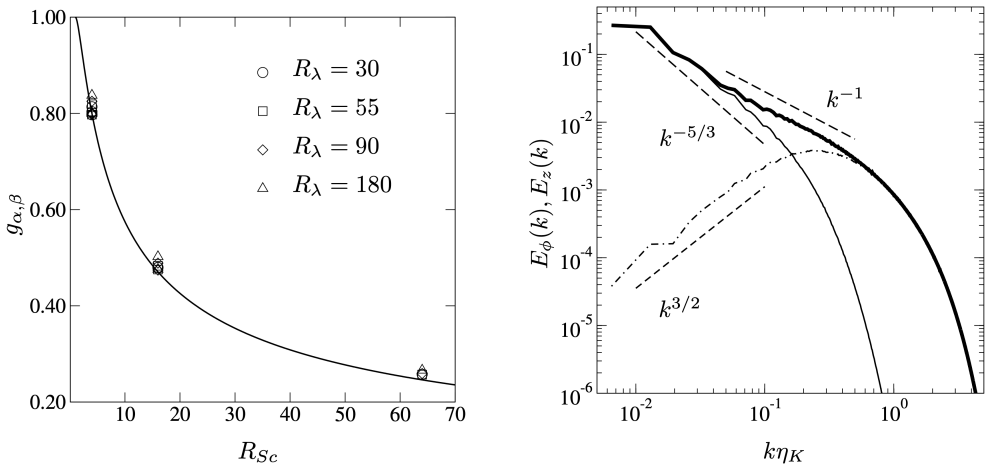

Figure 10: Statistical measures of the differential diffusion. Left picture: correlation coefficients of the gradients of different scalars, equation (18), as a function of R_{Sc} for various R_λ. The solid line shows the model given by equation (19). Right picture: Scalar variance spectra for scalars with $Sc = 12$ (thick line) and with $Sc = 3/16$ (thin line) and the spectrum of the associated scalar difference, z, variance (dotted-dashed line), for $R_\lambda = 180$.

with the higher Schmidt number (higher than 1) exhibits a viscous-convective range at the highest wave numbers. At these scales, the spectrum of the scalar difference perfectly follows the spectrum of the scalar with the highest Schmidt number, because there is no mixing at these scales for the scalar with the smallest Schmidt number [37]. At larger scales, the variance spectrum of z increases roughly as $k^{3/2}$, as already observed by Yeung [31]. This means that there is a peak for this spectrum characterizing the scales of the differential diffusion.

These results suggest to normalize the variance spectrum of the scalar difference with the Batchelor scaling based on the highest Schmidt number, as already proposed by Yeung *et al.* [33]. Figure 11 (left) shows the normalized variance spectra of the scalar difference for all the cases of the database. As expected, a good collapse is found for all the spectra for high enough wave numbers. Moreover, the normalized spectra are found independent of the Reynolds number. However, the collapse is only partial, because it depends on R_{Sc}. In particular, the spectrum peak of the differential diffusion process depends on R_{Sc}. The typical scale of the differential diffusion, noted l_p, is defined from the peak wavenumber. Figure 11 (right) shows the value of the

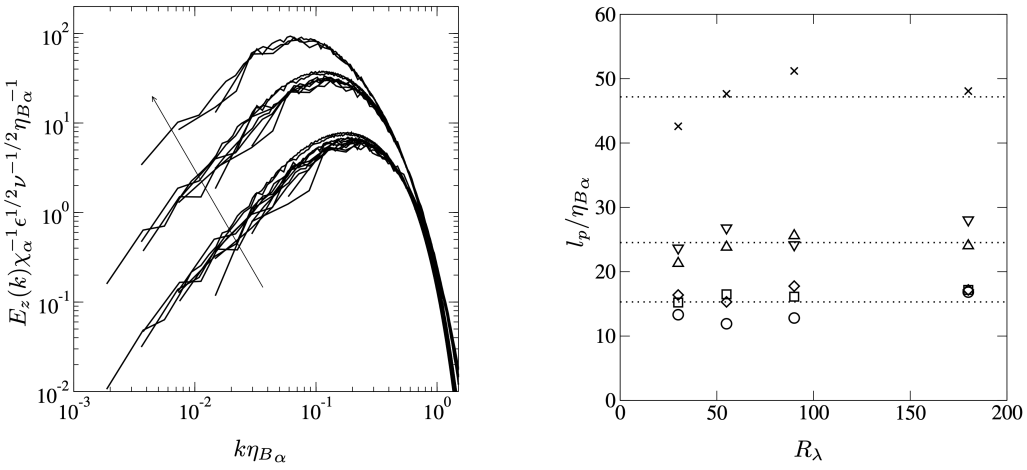

Figure 11: Left picture: variance spectra of the scalar difference for all the cases of the DNS database. The spectra are normalized by using the Batchelor scaling based on the highest Schmidt number. The arrow shows increasing values of R_{Sc}. Right picture: evolution of the ratio between the scale of the peak of the differential diffusion and the Bachelor scale of the scalar with the highest Schmidt number, l_p/η_{B_α}, as a function of R_λ for all the couples of scalars: $R_{Sc} = 4$ (3/16-3/4, square; 3/4-3, circle; 3-12, diamond), $R_{Sc} = 16$ with (3/16-3, triangle up; 3/4-12, triangle down) and $R_{Sc} = 64$ (cross). The dotted lines show the mean value computed at fixed R_{Sc}.

ratio between scale of the peak the differential diffusion, l_p, and the Bachelor scale of the scalar with the highest Schmidt number, η_{B_α}. This ratio, l_p/η_{B_α}, seems to only depend on R_{Sc}. This means that this typical scale is not directly linked with the large scales, but with the smallest scale of the less diffusive scalar.

4.2.3. Transfer of the differential diffusion phenomenon

As already mentioned, to deeper characterize the differential diffusion phenomenon, the transport equation of the square of the instantaneous scalar difference, z^2, equation (14) can be considered. Note that in the case of forced homogeneous isotropic turbulence, one can simplify Eqs. (16) and (17). Indeed, in this case $\langle z \rangle = 0$, and then, $\langle z'^2 \rangle = \langle z^2 \rangle$. Therefore, equation (16) can be dropped. Moreover, at steady state, equation (17) leads to

$$-2S\langle \nabla z \cdot \nabla z \rangle = -2D\langle \nabla z \cdot \nabla w \rangle, \tag{20}$$

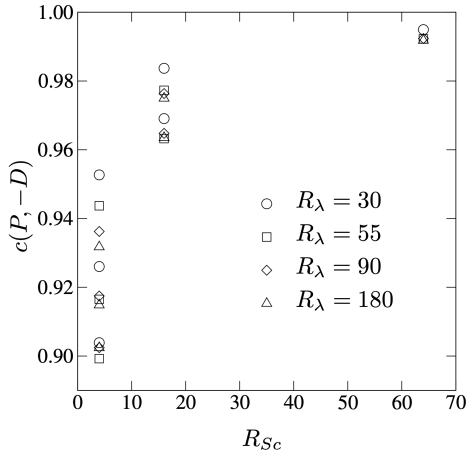

Figure 12: Correlation coefficient as a function of R_{Sc} between the opposite of the dissipation term, $-D$, and the production term, P, in equation (14).

showing that the global equilibrium between dissipation and production terms necessary holds in the considered flow configuration. To assess if the equilibrium acts also locally the correlation between the opposite of the dissipation term, $-D$, and the production term, P, appearing in the transport equation of z^2, equation (14), is shown by figure 12 for all the scalar differences of the database. The dissipation and the production terms are highly correlated with a coefficient correlation higher than 0.9. It is observed that the coefficient correlation increases with R_{Sc} and it is very close to 1 for $R_{Sc} = 64$. This means that the equilibrium is well verified, not only globally, but also locally, *i.e.* that $P = -D$ not only in average. This is confirmed by figure 13 showing the joint probability density function (J-PDF) between $-D$ and P, for two different couples of scalar at $R_\lambda = 180$. The J-PDF of exactly equal terms will be aligned on the $y = x$ line. This confirms the local equilibrium : the magnitude of the production and dissipation terms are very close locally, in particular for high R_{Sc}. Moreover, even if P is positive in average, it can be also observed that P can be locally negative, unlike $-D$ which is always positive by definition.

This suggests that the differential diffusion is a local phenomenon, and that the transfers between scales are weak. To better analyze the scales transfer of the differential diffusion phenomenon, spatial filtering is next used [43, 44]. The objective is to split the fields between large and small scales.

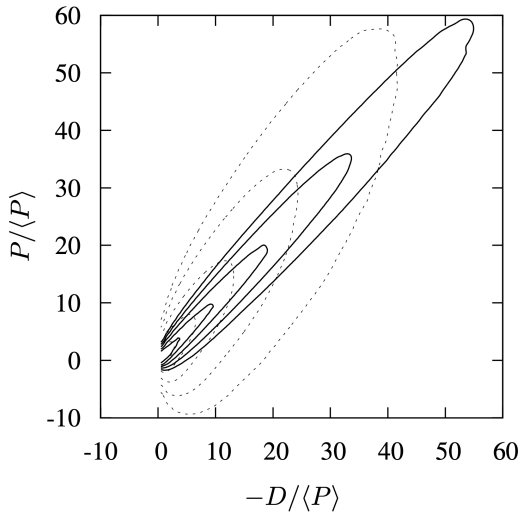

Figure 13: Joint probability density function (J-PDF) between the opposite of the dissipation term, $-D$ and production term, P, for $R_\lambda = 180$. The solid lines are for $R_{Sc} = 64$ ($Sc_1 = 12$ and $Sc_2 = 3/16$), whereas the dotted lines are for $R_{Sc} = 4$ ($Sc_1 = 3$ and $Sc_2 = 3/4$). The isocontours are in the range 10^{-6} to 10^{-2} with a logarithm scale.

This scales separation is performed by using the following filtering operation,

$$\bar{s}(\mathbf{x},t) = \int s(\mathbf{y},t) G_{\bar{\Delta}}(\mathbf{x}-\mathbf{y}) d\mathbf{y}, \tag{21}$$

with $\bar{s}$ the filtering of the field s, and $G_{\bar{\Delta}}$ the filter kernel with a filter size $\bar{\Delta}$. The scalar field, z, is then decomposed as a filter-scales (FS) field, $\bar{z}$, and a subfilter-scales (SFS) field. To better understand the FS/SFS interaction, the transport equation for $\bar{z}^2$ is written as,

$$\frac{\partial \bar{z}^2}{\partial t} = \nabla\cdot\big(S\nabla\bar{z}^2 + 2D\bar{z}\nabla\bar{w} - \bar{\mathbf{v}}\bar{z}^2 - 2\bar{z}\mathbf{T}\big) \underbrace{-2S\nabla\bar{z}\cdot\nabla\bar{z}}_{D^>} \underbrace{-2D\nabla\bar{z}\cdot\nabla\bar{w}}_{P^>} \underbrace{+2\mathbf{T}\cdot\nabla\bar{z}}_{T^>_<}, \tag{22}$$

with $\mathbf{T} = \overline{\mathbf{v}z} - \bar{\mathbf{v}}\bar{z}$, the SFS flux of the scalar difference. This allows to characterize the differential diffusion occurring at scales higher than the filter size, $\bar{\Delta}$. This equation is close to the equation obtained for the (full) scalar difference field, z^2, with diffusion terms written in the divergence form, SF dissipation term, $D^>$, and SF production term, $P^>$. There is also an additional term, $T^>_< = 2\mathbf{T}\cdot\nabla\bar{z}$, which represents the scales transfers from

the filter-scales to the subfilter-scales. These FS/SFS transfer terms can act as either a sink term for the FS field, meaning a transfer from FS to FSF (forward scatter), or as a source term, meaning an inverse transfer (backward scatter).

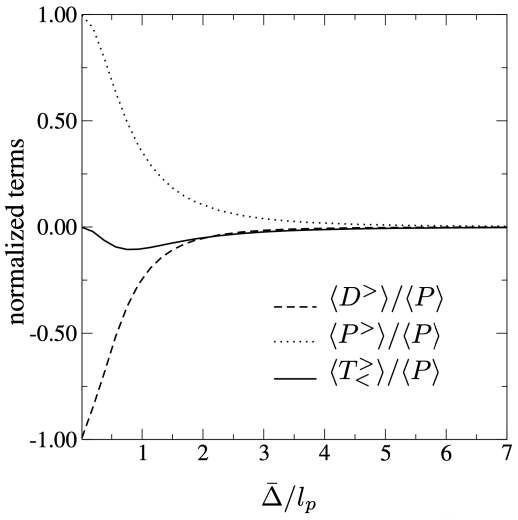

Figure 14: Evolution of the FS global equilibrium with the filter size for $R_\lambda = 180$ and $R_{Sc} = 4$ ($Sc_1 = 12$ and $Sc_2 = 3$). The filter size is normalized by the characteristic scale of the differential diffusion, l_p.

As already mentioned, the diffusion terms will be zero in average in the considered flow configuration. The FS global equilibrium is then between $\langle D^> \rangle$, $\langle P^> \rangle$ and $\langle T^>_< \rangle$. The evolution of the FS global equilibrium with the filter size is shown by figure 14 at $R_\lambda = 180$ and $R_{Sc} = 4$ ($Sc_1 = 12$ and $Sc_2 = 3$). In the previous section, the characteristic scale of the differential diffusion process, l_p, has been identified. The filter size is normalized by this scale. The case $\bar{\Delta}/l_p = 0$ corresponds to the non-filtered case, and the global equilibrium between dissipation and production is found. For larger filter size, the FS/SFS transfer term is no more zero. The magnitude of this term increases but this term is negative showing that there is mainly a transfer from large to small scale (direct transfer). This transfer is maximum around $\bar{\Delta}/l_p \approx 1$, confirming thus that l_p is the correct characteristic scale of the differential diffusion phenomenon. However, even at this filter size the mean FS/SFS transfer does not exceed 10% of the mean production. This confirms that the differential diffusion is mainly local phenomenon, with weak scales

transfers. Note that the three terms are almost zero for $\bar{\Delta}/l_p > 5$. This means that all the differential diffusion happens at subfilter-scales for $\bar{\Delta}/l_p > 5$, confirming that the differential diffusion is a small-scale phenomenon.

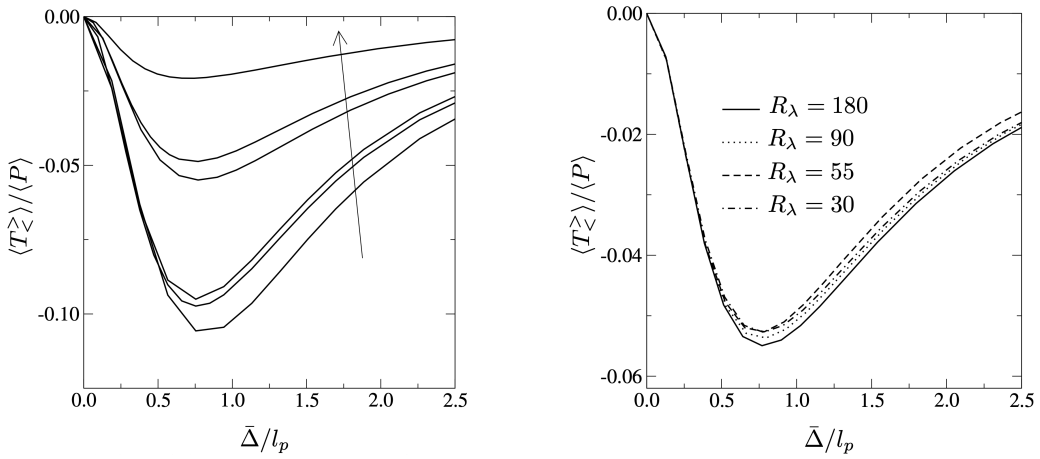

Figure 15: Evolution of the mean FS/SFS transfer term normalized by the mean production term as a function of the filter size normalized by the characteristic scale of the differential diffusion, l_p: at $R_\lambda = 180$ where the arrow indicates increasing values of R_{Sc} (left); at $R_{Sc} = 16$ for various R_λ (right).

Figure 15 shows the evolution of the mean FS/SFS transfer term with the filter size at a given R_λ, for various R_{Sc} (left) and at given R_{Sc}, for various R_λ (right). The ratio between the mean FS/SFS transfer and the total (unfiltered) production term appears to be only controlled by R_{Sc}. Indeed, this ratio is independent of the Reynolds number (Figure 15, right) and independent of the values of both Schmidt numbers (Figure 15, left). Moreover, the FS/SFS transfer decreases with the increase of R_{Sc}. This is consistant with the observation previously done showing a very high correlation between dissipation and production terms. This confirms that the differential diffusion is more and more local with increasing of R_{Sc}, with a very weak part of scales transfer.

4.3. Jet Flow

In this section we study the physics of differential diffusion in the flow created by a transitional round jet. We first specify the flow configuration.

We also define the grid resolution required for the velocity and the scalars, depending on the Schmidt numbers. We finally discuss the physics of differential diffusion based on a Reynolds decomposition.

4.3.1. Flow and grid configuration

To now study the differential diffusion in flow configuration with a mean field, a round jet in transition to turbulence is considered. The flow configuration is defined by its inlet velocity profile. At the inlet, the mean velocity field is non zero only for the streamwise component, which is given by a hyperbolic tangent profile [45] :

$$u_{\text{ref}}(\mathbf{x}) = \frac{U_1 + U_2}{2} - \frac{U_1 - U_2}{2} \tanh\left(\frac{R}{4\Gamma_0}\left(\frac{r}{R} - \frac{R}{r}\right)\right),$$

where U_1 is the centerline velocity, U_2 is a small co-flow, Γ_0 is the momentum thickness of the initial shear layer, r the radial coordinates (taking the origin at the center of the jet), and R the initial jet radius. The Reynolds number is fixed at a moderate value, $Re = U_1 R/\nu = 1500$. To accelerate the transition a forcing term is added. This forcing is first composed by a random part only added in the shear layer of the jet to the three velocity components. It follows a Passot-Pouquet spectrum with an amplitude set to 10% of U_1. For the streamwise component, the forcing is then complemented by a deterministic part, which consists in a varicose (axisymetric) excitation [46],

$$u_{\text{df}}(\mathbf{x}, t) = \epsilon u_{\text{ref}}(\mathbf{x}) \sin\left(2\pi St_R \frac{U_1 + U_2}{2\Gamma_0} t\right)$$

with a forcing amplitude $\epsilon = 2.5\%$, and St_R fixed at 0.033 to trigger the frequency predicted by the linear stability theory [45].

To consider the differential diffusion process in this flow configuration, two scalars are seeded in the jet with a hyperbolic tangent profile similar to the streamwise velocity, with the scalar value equal to 1 in the jet and zero in the outer region. The scalars only differ by their molecular diffusivity, leading to Schmidt numbers 0.8 and 8. The scalars will be denoted by $\theta_{0.8}$ and θ_8, respectively.

Unlike in the previous case, this configuration cannot be handled by a spectral method for the Navier-Stokes equations. The hybrid method described in section 2 coupling finite-volume method and a semi-lagrangian particle method is instead used. This allows also to consider distinct computational

domains for the flow and scalar dynamics. For the flow dynamics, the domain is a parallelepiped with size $20R \times 14R \times 14R$ in the streamwise and the two transverse directions, respectively. The size of the transverse directions are large enough to allow the flow rate added by the co-flow to be larger than the flow rate entrainment of the jet. An homogeneous spatial resolution is used in the core of the jet, that is where vorticity is not negligible, with a cell size $\Delta \approx 0.375R$ which is the typical mesh size used for similar configuration at similar Reynolds number [47]. Outside the core of the jet, the mesh is unrefined to limit the number of cells. Overall, the mesh consists of 50 millions tetrahedra.

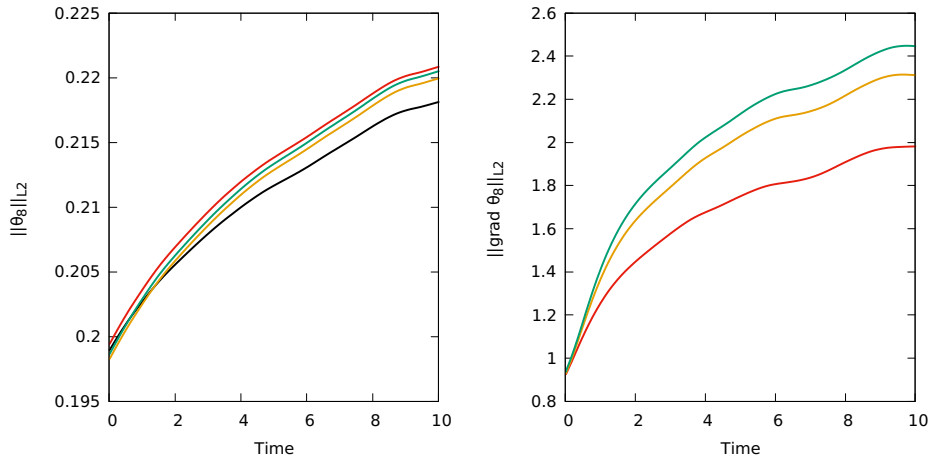

Figure 16: Evolution of L^2-norm of θ_8 (left) and $\nabla\theta_8$ (right) after scalar initialization and over $t = 10U_1/R$. Finite-volume method with mesh size Δ in the core (black curve) and hybrid method with grid size Δ (red curves), $\Delta/2$ (magenta curve) and $\Delta/4$ (green curve).

For the advection of scalars, the domain is a smaller parallelepiped with size $20R \times 5R \times 5R$ in streamwise and both transverse directions. Choosing smaller transverse sizes than for the finite-volume solver amount to choosing homogeneous Dirichlet conditions on the lateral boundaries. This has a negligible effect on the dynamics of the scalar as the box is big enough so that the flow is mostly outgoing at these edges. Note that the semi-lagrangian method, unlike eulerian methods, does not face issues related to possible spurious reflections at boundaries.

To choose the grid size in the particle box, we have undertaken the following refinement study that can also serve as an accuracy check for the hybrid method. We considered the more challenging value $Sc = 8$ and first

looked at the energy norm of the scalar θ_8, using either the hybrid method or the pure finite-volume method, for grid sizes Δ, $\Delta/2$ and $\Delta/4$, where we recall that Δ is the mesh size of the finite-volume mesh in the core of the jet. The results, shown on the left picture of Figure 16, show that, unlike the pure finite-volume method, the hybrid method gives converged results for the RMS of θ, with the grid size Δ. However, to obtain reliable values for the different diagnostics presented below, it is also desirable to have accurate values for the scalar gradients. The bottom picture of Figure 16 shows that the grid size Δ for the hybrid method is not sufficient and a grid size $\Delta/2$, although not yet converged, was found to give reasonable accuracy. This grid size corresponds to a particle mesh with $1068 \times 268 \times 268$ points.

4.3.2. Computational cost

Let us now discuss the computational efficiency of the method.

The simulations were carried out on 840 cores of the Occigen machine of the Cines made of xeon E5 cores running at 2.6GHz.

To simulate a scalar with a Schmidt number $Sc = 8$, the hybrid solver takes 2.4s of wall-clock time per time step for a grid size $\Delta/2$. The pure finite-volume method using the same grid-size in the core of the jet, which, as we have seen earlier, would not be enough to achieve the same level of accuracy, and a time-step twice smaller due to the CFL condition, would require 4s to reach the same physical time.

However, the efficiency obtained in this configuration for the hybrid method is not quite inline with the timings shown in 3. A simple extrapolation from the results of Table 1, assuming perfect scalability, would give a wall-clock time of about 0.7s per iteration. This discrepancy is due to a domain partitioning leading to a poor load-balancing in the jet configuration.

For load balancing in the finite-volume solver, the computational domain can be roughly divided into 3 zones. In the core of the jet, the velocity mesh is uniform as already mentioned. Good load balancing can thus be achieved for both the finite-volume and particle solvers. A second zone is located near the lateral edges of the domains. In this area the scalar values are small or zero. This area is therefore mostly void of particles. Although the size of the velocity cells are much bigger than the size of the particle cells, in this area particles do not deteriorate the load balancing. Finally there is a third intermediate zone with large velocity scales associated to large cells of the finite-volume mesh. Here, the ratio between the computational load of the semi-lagrangian solver and the finite-volume solver increases significantly.

For the moment, it has not been possible to obtain an acceptable domain partitioning with METIS leading to satisfactory load balancing for both the finite-volume and particle solvers.

4.3.3. Instantaneous pictures of the flow dynamics and the differential diffusion

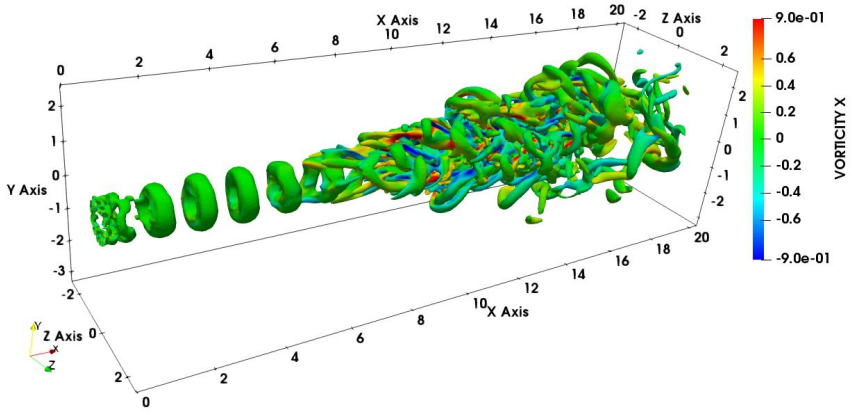

Figure 17: Iso-surface of the Q-Criterion for $Q = 0.1(U_1/R)^2$ colored by the streamwise vorticity ω_x.

The mixing of scalars is mainly dominated by the flow dynamics during the transition process through laminar to turbulent flow. The main structures of the flow dynamics can be observed using the Q-Criterion [48, 49]. This value is a good indicator of presence of vortices. Figure 17 shows the iso-surface $Q = 0.1(U_1/R)^2$. The classical rings created by Kelvin-Helmholtz instabilities can be found until $x/R < 8$. Beyond $x/R = 10$, there is an abrupt increase in the level of small-scales turbulence due to the appearance of pairs of streamwise vortices between two consecutive primary vortices in agreement with the classical scenario of transition in free shear layers.

To give now a qualitative illustration of the mixing phenomena, instantaneous contours of scalars in the central plane are shown on figure 18. The turbulent mixing activity emerges soon as far as coherent structures become extensive. Thus, the turbulent mixing starts with an engulfment of the two jet fluids through the shear layers implied by the Kelvin–Helmholtz vortices.

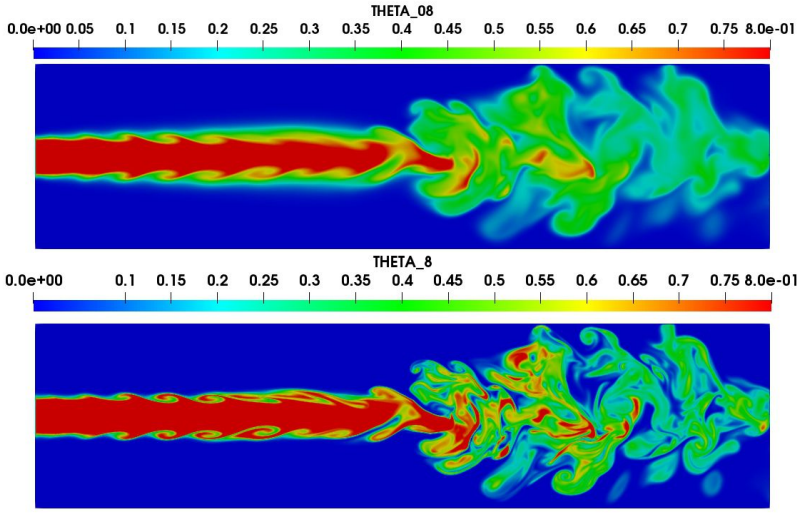

Figure 18: Instantaneous contours of scalars in the central plane for $\theta_{0.8}$ (top) and θ_8 (bottom).

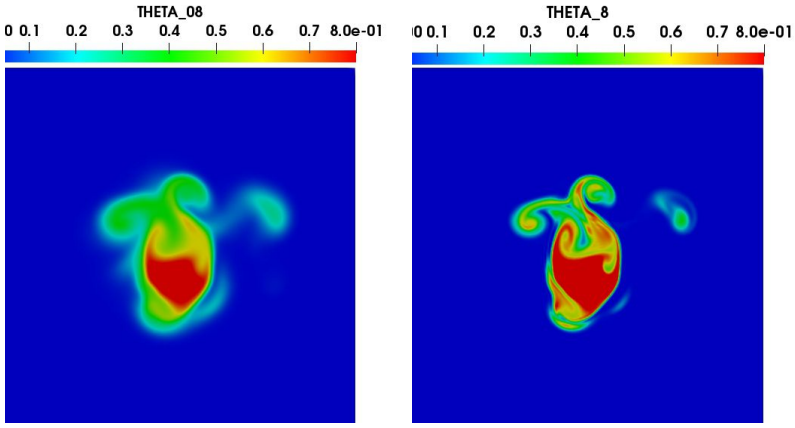

Figure 19: Instantaneous contours of scalars in the plane $x/R = 10$ for $\theta_{0.8}$ (left) and θ_8 (right).

With the appearance of the three-dimensional vortices, ejections of space-coherent packets of scalars into the ambient fluid appear, leading to the mushroom-shaped tracer structures, as shown by figure 19. For $x/R > 10$, the mixing finally occurs in the core of the jet.

The effect of molecular diffusivities clearly appears on these figures. Whereas thin layers of scalar exist for the scalar θ_8, with a Schmidt number equal to 8, they are quickly removed by diffusion effect for the scalar $\theta_{0.8}$, with a Schmidt number equal to 0.8. These thin layers for θ_8 are mainly visible in the core of the Kelvin-Helmholtz vortices and in the three-dimensional vortices.

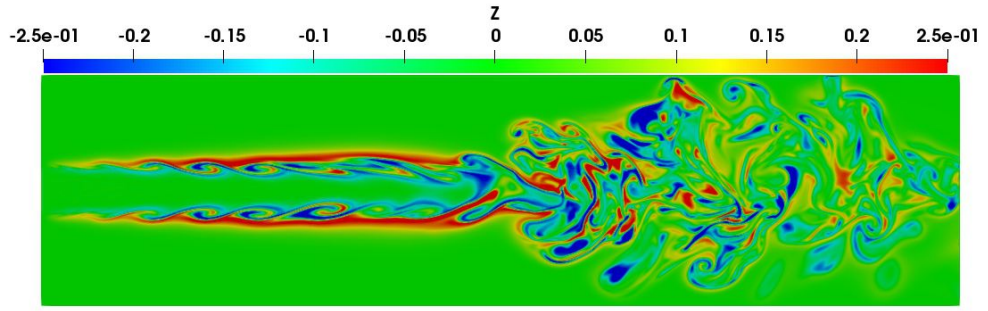

Figure 20: Instantaneous contours of $z = \theta_{0.8} - \theta_8$ in the central plane

To characterize the differential diffusion process, Fig. 20 shows the instantaneous contours of the scalar difference, $z = \theta_{0.8} - \theta_8$, in the central plane. As expected, z is first different to zero only at the turbulent/non turbulent (T/NT) interface [6] at the beginning of the transition process. The differential diffusion occurs in the core of the jet, simultaneously with the appearance of the three-dimensional vortices. Figure 21 shows the dissipation and production terms identified in the transport equation of z^2, equation (14), in the central plane. Similarly to the isotropic turbulent configuration, it seems that the two terms are highly correlated, showing that a local (in space and time) equilibrium occurs between the dissipation and the production for the differential diffusion process.

4.3.4. Analysis of the differential diffusion based on Reynolds decomposition

To deeper characterize the effect of turbulence, the Reynolds decomposition can be adopted to distinguish the mean field, $\langle z \rangle$, and the turbulent field, $z_{\text{rms}} = \sqrt{\langle z'^2 \rangle}$. Fig 22 (a) shows $\langle z \rangle$ in the mid-plane of the jet. At the beginning of the jet, $\langle z \rangle$ is non zero only in the shear layer due to the diffusion difference. Turbulent mixing due to the appearance of the Kelvin-Helmholtz vortices leads to an important radial growth of the phenomenon until the

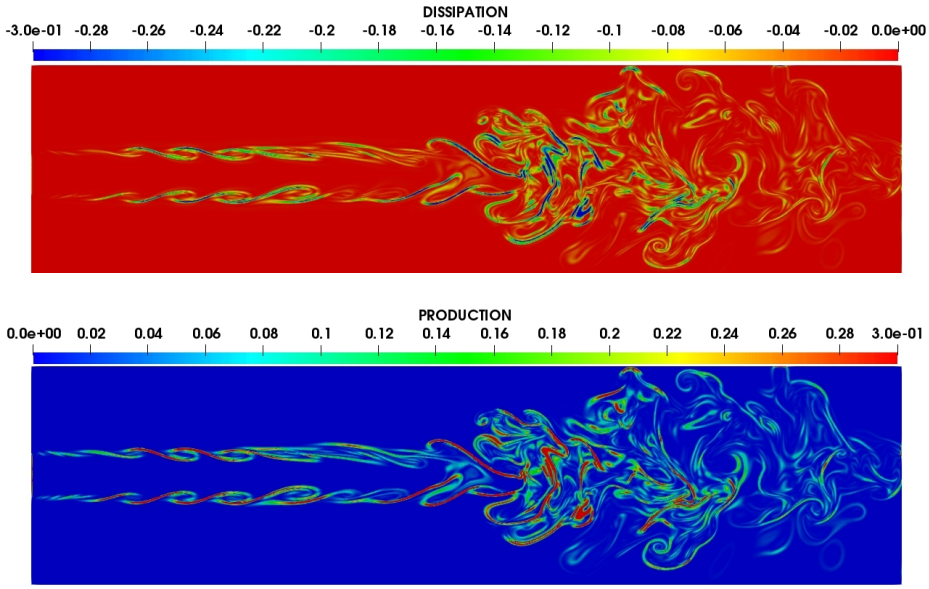

Figure 21: Instantaneous contours of Dissipation (top) and Production (bottom) terms from 14 in the central plane.

middle of the jet. For $x/R > 10$, i.e. at the end of the potential core, $\langle z \rangle$ is zero everywhere, which means that differential diffusion only persists in the turbulent field. This is confirmed by Fig 22(b) which shows z_{rms} in the mid-plane of the jet. As expected differential diffusion in the turbulent field starts with the appearance of the Kelvin-Helmholtz vortices, and it is then located in the shear layer. At the end of the potential core, when the differential diffusion disappears of the mean field, it is dominant in the center of the jet for the turbulent field, and the phenomenon persists until the end of the domain. The distribution of z_{rms} is similar as the distribution of the turbulent kinetic energy [50]. In particular maximum values of z_{rms} occur within the shear layer just downstream of the location of potential core breakdown.

Similarly to the analysis proposed by Anghan et al. [50] on the turbulent kinetic energy budget, the main mechanisms leading to the observed distribution for the mean field, $\langle z \rangle$, and the turbulent field, z_{rms} can be given by looking at the budget equations (16) and (17). Figure 23 shows the radial profile of the terms of the budget of the mean field, equation (16), namely diffusion, dissipation, production and transfer terms. The production of

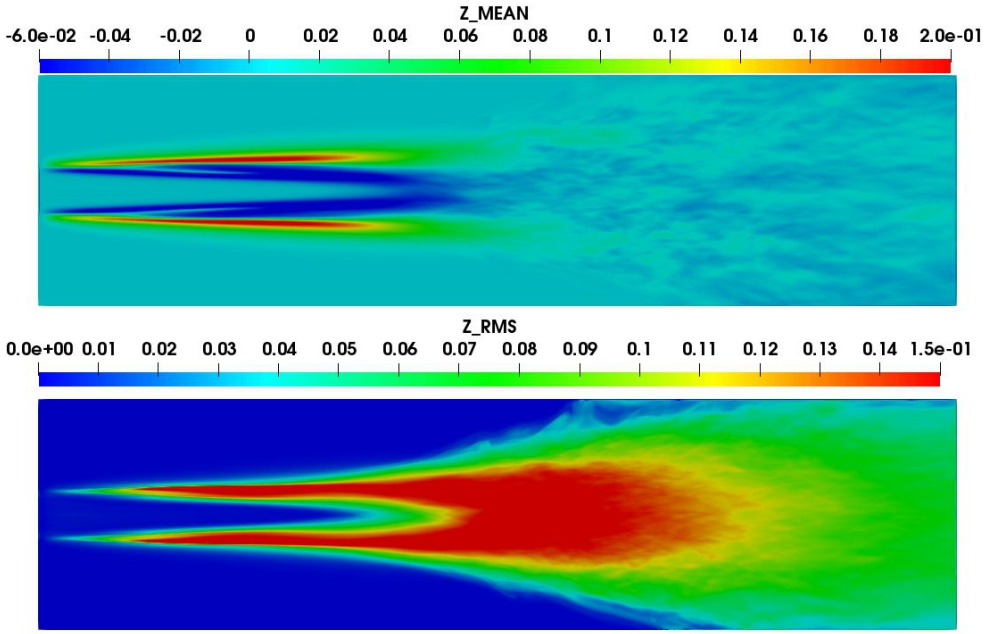

Figure 22: Value of $\langle z \rangle$(top) and z_{rms}(bottom) in the mid-plane.

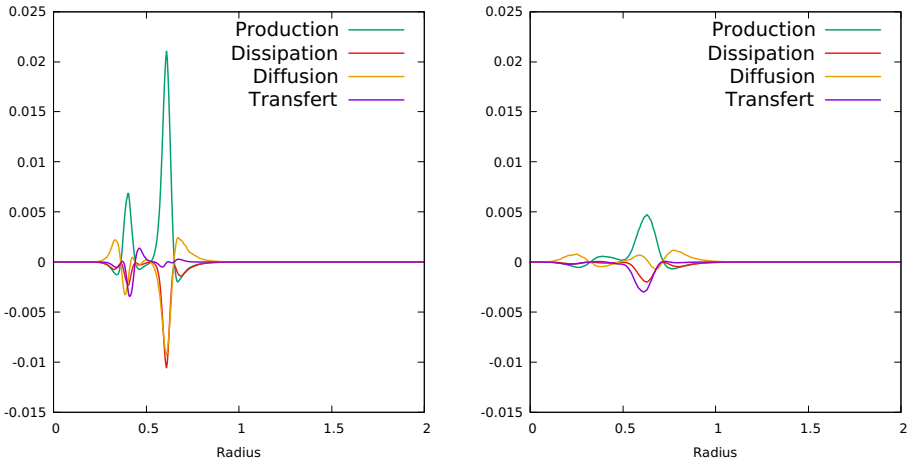

Figure 23: Budget of $\langle z \rangle^2$, equation (16). Radial profile at $x/R = 3$ (left), and 6 (right).

differential diffusion in the mean field mainly occurs in the edges of the shear layer. The production is mostly balanced by diffusion and dissipation. The

transfer term is mainly negative, showing that the transfer occurs from the mean field to the turbulent field. However, the transfer term is one order of magnitude below the other terms, showing that this term does not have a significant influence on the mean field.

Going downstream, the magnitude of the peaks of production vanishes to zero. Downstream of $x/R = 6$, the transfer term becomes comparable to the other terms, but in this zone the differential diffusion mainly occurs in the turbulent fields. It can be noted that the production term has a negative value close to the production peaks, which are mainly compensated by the diffusion process, showing that the diffusion essentially consists in spreading from the production region towards the center of the jet and the non-turbulent region. Figure 24 shows the radial profile of the terms of the budget of the turbulent field, equation (17). The transfer term is the opposite of the term appearing in the mean field budget. However, this term is clearly dominated by production and dissipation terms, showing that there is a decoupling between mean and turbulent field for the differential diffusion phenomenon. Moreover, from the first step of the transition process until the full turbulent state, the diffusion is also clearly dominated by the production and dissipation terms. There is a clear equilibrium between these two terms. Note that this equilibrium is expected at the end of the jet, where $\langle z \rangle \approx 0$, as already discussed for the HIT case, equation (20). But the equilibrium assumption is also valid at the beginning of the jet. It seems even valid for the instantaneous field as previously shown by Figure 21.

5. Conclusion

Thanks to an hybrid method combining an eulerian (either pseudo-spectral of finite-volume) method and a second order semi-lagrangian particle method with good parallel scalability, we were able to study differential diffusion at a reasonable computational cost for Schmidt numbers that were not previously reported. The hybrid method was validated both form the point of view of accuracy and computational efficiency against a purely finite-volume method.

This method allowed us to perform a numerical study of the differential diffusion phenomenon in homogeneous isotropic turbulence and in a transitional round jet. By studying quantities based on scalar difference, it has been observed that the transfer between mean and turbulent fields is weak, and, furthermore, that the scales transfers for the turbulent field are limited.

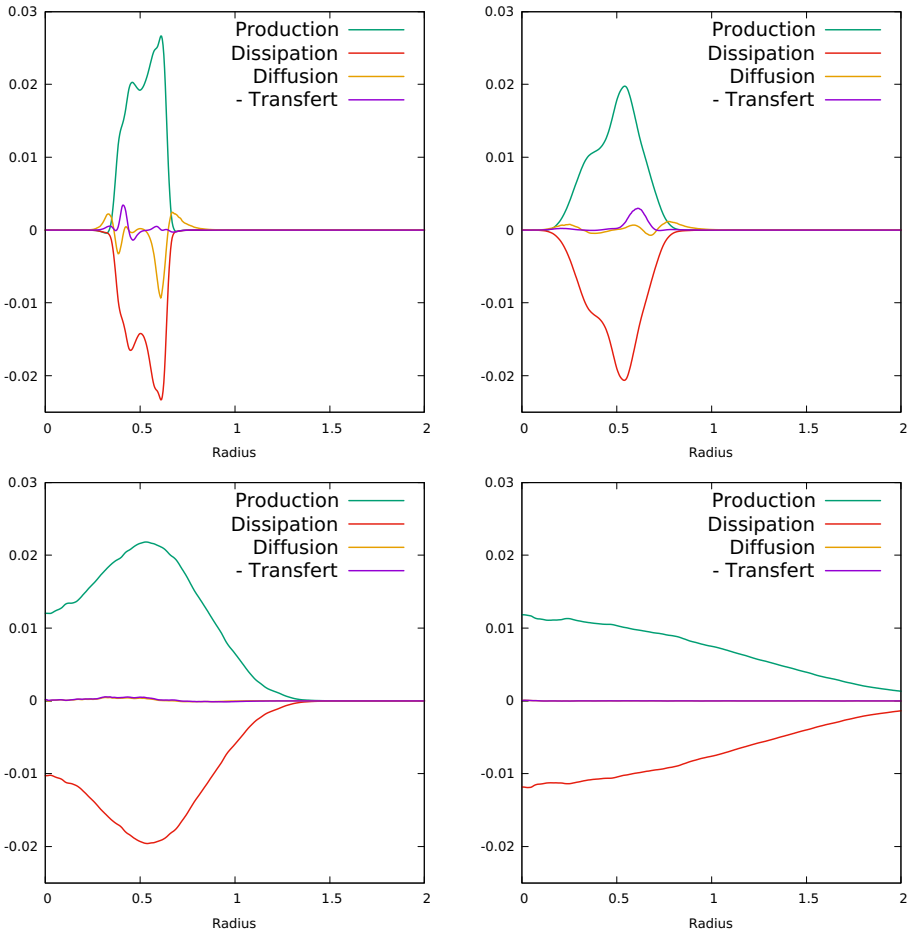

Figure 24: Budget of $\langle z'^2 \rangle$ as given by equation (17). Radial profile at $x/R = 3$ (top left), 6(top right), 9 (bottom left), and 15 (bottom right).

This confirms previous studies showing that the differential diffusion is a local phenomenon in space and time.

Simulations made in the jet configuration showed that there is room for improvement in the load balancing for the hybrid finite-volume / particle method. Difficulties arose from domain partitioning solely based on the finite-volume solver. In the future we plan to experiment with alternative parallel strategies. The domain decomposition for each of the meshes, unstructured mesh for the velocity and cartesian mesh for the scalars, will be performed separately. The velocity field, computed on the unstructured mesh, will then

have to be communicated to the processors in charge of transporting the scalar field. With such an approach we expect the load balancing to be optimized independently on the two process pools used for velocity and scalar calculations.

Future works will also include the extension of the hybrid method to the coupling of the finite-volume method with multi-resolution particle method as described in [20]. This should allow to increase the local density of particles and therefore to address even higher Schmidt numbers.

Acknowledgements

The authors gratefully acknowledge support from *Programme Investissement d'Avenir* under grant ANR-17-CE23-0024-01. Computations were performed using HPC resources from GENCI (Grants 020611).

References

[1] Andrey Pushkarev, Guillaume Balarac, and Wouter JT Bos. Reynolds and prandtl number scaling of viscous heating in isotropic turbulence. *Physical Review Fluids*, 2(8):084606, 2017.

[2] I. Calmet and J. Magnaudet. High-schmidt number mass transfer through turbulent gas–liquid interfaces. *International Journal of Heat and Fluid Flow*, 19:522–532, 1998.

[3] Heinz Pitsch, Olivier Desjardins, Guillaume Balarac, and Matthias Ihme. Large-eddy simulation of turbulent reacting flows. *Progress in Aerospace Sciences*, 44(6):466–478, 2008. Large Eddy Simulation - Current Capabilities and Areas of Needed Research.

[4] J. A. Sethian and Peter Smereka. Level set methods for fluid interfaces. *Annual Review of Fluid Mechanics*, 35(1):341–372, 2003.

[5] M. Lesieur. *Turbulence in fluids*. Springer,Dordrecht, 2008.

[6] F. Hunger, M. Gauding, and C. Hasse. On the impact of the turbulent/non-turbulent interface on differential diffusion in a turbulent jet flow. *Journal of Fluid Mechanics*, 802:R5, 2016.

[7] D.A. Donzis and P.K. Yeung. Resolution effects and scaling in numerical simulations of passive scalar mixing in turbulence. *Physica D: Nonlinear Phenomena*, 239(14):1278 – 1287, 2010. At the boundaries of nonlinear physics, fluid mechanics and turbulence: where do we stand? Special issue in celebration of the 60th birthday of K.R. Sreenivasan.

[8] T. Gotoh, S. Hatanaka, and H. Miura. Spectral compact difference hybrid computation of passive scalar in isotropic turbulence. *Journal of Computational Physics*, 231(21):7398 – 7414, 2012.

[9] J.-B. Lagaert, G. Balarac, and G.-H. Cottet. Hybrid spectral-particle method for the turbulent transport of a passive scalar. *Journal of Computational Physics*, 260:127 – 142, 2014.

[10] R. Ostilla-Monico, Yantao Yang, E.P. van der Poel, D. Lohse, and R. Verzicco. A multiple-resolution strategy for direct numerical simulation of scalar turbulence. *Journal of Computational Physics*, 301:308–321, 2015.

[11] Vincent Moureau, Pascale Domingo, and Luc Vervisch. Design of a massively parallel cfd code for complex geometries. *Comptes Rendus Mécanique*, 339(2):141 – 148, 2011. High Performance Computing.

[12] Z. Warhaft. Passive scalars in turbulent flows. *Annual Review of Fluid Mechanics*, 32(1):203–240, 2000.

[13] Paul E. Dimotakis. Turbulent mixing. *Annual Review of Fluid Mechanics*, 37(1):329–356, 2005.

[14] R.W. Bilger. Reaction rates in diffusion flames. *Combustion and Flame*, 30:277 – 284, 1977.

[15] T. M. LAVERTU, L. MYDLARSKI, and S. J. GASKIN. Differential diffusion of high-schmidt-number passive scalars in a turbulent jet. *Journal of Fluid Mechanics*, 612:439–475, 2008.

[16] G.H. Cottet and P. Koumoutsakos. *Vortex methods*. Cambridge University Press, 2000.

[17] G. S. Winckelmans. Vortex methods. *Encyclopedia of Computational Mechanics*, 3, 2004.

[18] P. Koumoutsakos. Multiscale flow simulations using particles. *Annual Review of Fluid Mechanics*, 37(1):457–487, 2005.

[19] G.-H. Cottet, J.-M. Etancelin, F. Perignon, and C. Picard. High order semi-lagrangian particle methods for transport equations: numerical analysis and implementation issues. *ESAIM: Mathematical Modelling and Numerical Analysis*, 48(4):1029–1060, 2014.

[20] Michael Bergdorf and Petros Koumoutsakos. A lagrangian particle-wavelet method. *Multiscale Modeling & Simulation*, 5(3):980–995, 2006.

[21] Michael Bergdorf, Georges-Henri Cottet, and Petros Koumoutsakos. Multilevel adaptive particle methods for convection-diffusion equations. *SIAM Multiscale Modeling and Simulation*, 4:328–357, 2005.

[22] Manuel Bernard, Ghislain Lartigue, Guillaume Balarac, Vincent Moureau, and Guillaume Puigt. A framework to perform high-order deconvolution for finite-volume method on simplicial meshes. *International Journal for Numerical Methods in Fluids*, 92(11):1551–1583, April 2020.

[23] Alexandre Chorin. Numerical solution of the navier–stokes equations. *Mathematics of Computation*, 22, 10 1968.

[24] Matthias Kraushaar. *Application of the compressible and low-mach number approaches to large-eddy simulation of turbulent flows in aero-engines*. Theses, Institut National Polytechnique de Toulouse, 12 2011.

[25] V. Moureau, C. Bérat, and H. Pitsch. An efficient semi-implicit compressible solver for large-eddy simulations. *Journal of Computational Physics*, 226(2):1256 – 1270, 2007.

[26] Mathias Malandain, Nicolas Maheu, and Vincent Moureau. Optimization of the deflated conjugate gradient algorithm for the solving of elliptic equations on massively parallel machines. *Journal of Computational Physics*, 238:32 – 47, 2013.

[27] Yann Dufresne, Vincent Moureau, Ghislain Lartigue, and Olivier Simonin. A massively parallel cfd/dem approach for reactive gas-solid flows in complex geometries using unstructured meshes. *Computers and Fluids*, 198:104402, 2020.

[28] J. R. Saylor and K. R. Sreenivasan. Differential diffusion in low reynolds number water jets. *Physics of Fluids*, 10(5):1135–1146, 1998.

[29] L.L. Smith, R.W. Dibble, L. Talbot, R.S. Barlow, and C.D. Carter. Laser raman scattering measurements of differential molecular diffusion in turbulent nonpremixed jet flames of h2co2 fuel. *Combustion and Flame*, 100(1):153 – 160, 1995.

[30] P. K. Yeung. Multi-scalar triadic interactions in differential diffusion with and without mean scalar gradients. *Journal of Fluid Mechanics*, 321:235–278, 1996.

[31] PK Yeung. Correlations and conditional statistics in differential diffusion: Scalars with uniform mean gradients. *Physics of Fluids*, 10(10):2621–2635, 1998.

[32] Vebjo/rn Nilsen and George Kosály. Differentially diffusing scalars in turbulence. *Physics of Fluids*, 9(11):3386–3397, 1997.

[33] PK Yeung, Michelle C Sykes, and Prakash Vedula. Direct numerical simulation of differential diffusion with schmidt numbers up to 4.0. *Physics of Fluids*, 12(6):1601–1604, 2000.

[34] P. K. Yeung and S. B. Pope. Differential diffusion of passive scalars in isotropic turbulence. *Physics of Fluids A: Fluid Dynamics*, 5(10):2467–2478, 1993.

[35] Rodney O Fox. The lagrangian spectral relaxation model for differential diffusion in homogeneous turbulence. *Physics of Fluids*, 11(6):1550–1571, 1999.

[36] W Bilger and RW Dibble. Differential molecular diffusion effects in turbulent mixing. *Combustion Science and Technology*, 28(3-4):161–172, 1982.

[37] AR Kerstein, MA Cremer, and PA McMurtry. Scaling properties of differential molecular diffusion effects in turbulence. *Physics of Fluids*, 7(8):1999–2007, 1995.

[38] C. Brownell and L. Su. Planar laser imaging of differential molecular diffusion in gas-phase turbulent jets. *Physics of Fluids - PHYS FLUIDS*, 20, 03 2008.

[39] PK Yeung. Multi-scalar triadic interactions in differential diffusion with and without mean scalar gradients. *Journal of Fluid Mechanics*, 321:235–278, 1996.

[40] K. Alvelius. Random forcing of three-dimensional homogeneous turbulence. *Phys. Fluids*, 11:1880–1889, 1999.

[41] S. B. Pope. *Turbulent Flows*. Cambridge Univ. Press, 2000.

[42] V. Eswaran and S.B. Pope. Direct numerical simulations of the turbulent mixing of a passive scalar. *Phys. Fluids*, 31:506–520, 1988.

[43] Carlos Bettencourt da Silva and Olivier Métais. On the influence of coherent structures upon interscale interactions in turbulent plane jets. *Journal of Fluid Mechanics*, 473:103–145, 2002.

[44] Mouloud Kessar, Guillaume Balarac, and Franck Plunian. The effect of subgrid-scale models on grid-scale/subgrid-scale energy transfers in large-eddy simulation of incompressible magnetohydrodynamic turbulence. *Physics of Plasmas*, 23(10):102305, 2016.

[45] Alfons Michalke and Gunter Hermann. On the inviscid instability of a circular jet with external flow. *Journal of Fluid Mechanics*, 114:343–359, 1982.

[46] Carlos B. da Silva and Olivier Métais. Vortex control of bifurcating jets: A numerical study. *Physics of Fluids*, 14(11):3798–3819, 2002.

[47] Lola Guedot, Ghislain Lartigue, and Vincent Moureau. Design of implicit high-order filters on unstructured grids for the identification of large-scale features in large-eddy simulation and application to a swirl burner. *Physics of Fluids*, 27:045107, 04 2015.

[48] J. Hunt, Alan Wray, and Parviz Moin. Eddies, streams, and convergence zones in turbulent flows. *Studying Turbulence Using Numerical Simulation Databases*, -1:193–208, 11 1988.

[49] Yves Dubief and Franck Delcayre. On coherent-vortex identification in turbulence. *Journal of Turbulence - J TURBUL*, 1, 12 2000.

[50] Chetan Anghan, Sagar Dave, Shaswat Saincher, and Jyotirmay Banerjee. Direct numerical simulation of transitional and turbulent round jets: Evolution of vortical structures and turbulence budget. *Physics of Fluids*, 31:065105, 06 2019.